Limitations in photoionization of helium by an extreme ultraviolet optical vortex

T. Kaneyasu,[1] Y. Hikosaka,[2] M. Fujimoto,[3,4] T. Konomi,[3,4] M. Katoh,[3,4] H. Iwayama,[3,4] and E. Shigemasa[3,4]

[1]*SAGA Light Source, Tosu 841-0005, Japan*
[2]*Graduate School of Medicine and Pharmaceutical Sciences, University of Toyama, Toyama 930-0194, Japan*
[3]*UVSOR Facility, Institute for Molecular Science, Okazaki 444-8585, Japan*
[4]*Sokendai (The Graduate University for Advanced Studies), Okazaki 444-8585, Japan*

Photoelectron angular distributions from helium atoms are measured using the circularly polarized extreme ultraviolet (XUV) vortex produced by a helical undulator as the higher harmonics of its radiation. The XUV vortex has a helical wave front and carries orbital angular momentum as well as the spin angular momentum associated with its circular polarization. While the violation of the electric dipole transition rules has been predicted for interactions between vortices and atoms, the photoelectron angular distributions are well reproduced by assuming electric dipole transitions only. This observation can be explained by the localized nature of the helical phase effect of the vortex on the interaction with atoms, and demonstrates that nondipole interactions induced by the XUV vortex are hardly observable in conventional gas-phase experiments.

I. INTRODUCTION

A photon beam having a helical wave front carries orbital angular momentum (OAM) as well as the spin angular momentum associated with its circular polarization. Since the pioneering work by Allen *et al.* [1], the characteristics of photon beams carrying OAM, which are usually referred to as optical vortices or twisted light, have been investigated both from the fundamental point of view, and for applicational purposes, such as optical data transmission [2], manipulation of small particles [3], coronagraphy [4], and high-resolution fluorescence microscopy [5]. Until now, the production and application of OAM beams have been mainly limited to the visible and infrared wavelength regions, where photon beams with helical wave fronts can be obtained using various optical elements [6]. In contrast, only a few experimental studies on OAM beams have been performed in the x-ray wavelength regions [7–9], because it is generally difficult to fabricate precise optical elements, necessary for producing helical wave fronts, which operate at short wavelengths.

Recently, it was found that the nth harmonic off-axis radiation from a helical undulator carries an OAM of $(n - 1)\hbar$ per photon [10–13], as a result of the spiral motion of electron which naturally emits an electromagnetic wave with a helical wave front [14]. This suggests the possibility of directly and efficiently producing a circularly polarized photon beam that carries OAM over the whole wavelength range covered by synchrotron light sources, from the VUV to hard x rays. This novel feature of helical undulator radiation will allow us to utilize OAM beams at short wavelengths, and may open up new applications specific to the remarkable properties of OAM carried by photon beams, as demonstrated at visible and infrared wavelengths.

In exploring new applications of OAM beams at short wavelengths, a fundamental understanding of the role of the OAM in the light-matter interaction is crucial. In recent years, several theoretical works have been reported on the photoionization and photoexcitation of atoms by OAM-carrying photons [15–19]. Differing from plane-wave photons, a violation of the standard electric dipole selection rules is

predicted for OAM-carrying photons, as a consequence of the transference of the OAM to the internal degrees of freedom of the atom [15,19]. In the x-ray regime, the use of electric quadrupole transitions induced by the OAM was proposed for dichroism experiments [20]. In contrast to these advances in theory, to our knowledge, there has been no experimental work on OAM light-matter interactions in the short wavelength regime, owing to the technical difficulty of producing brilliant and energy-tunable OAM beams. In this paper, we report the experimental investigation on the photoionization of helium atoms irradiated with a circularly polarized extreme ultraviolet (XUV) vortex beam produced by a helical undulator and discuss the limitations due to the experimental arrangement for studying the specific features of the OAM light-matter interaction. The interaction between OAM-carrying photons and atoms is tested by measuring photoelectron angular distributions, which are characterized by the angular momentum of the final state of the photoionization transition.

II. EXPERIMENT

The experiment was carried out at the undulator beamline BL1U of the 750-MeV UVSOR storage ring. The storage ring was operated in single-bunch mode, providing light pulses with a repetition period of 178 ns. The stored electron beam current was less than 1 mA. BL1U is a beamline originally dedicated to light source development, using undulator U1 which consists of twin APPLE-II type devices. The generation of an optical vortex using the U1 undulator was already verified in the UV wavelength region [12,13]. The XUV vortex can be obtained by tuning the pole gap of the undulator magnets. We measured photoelectron angular distributions from helium atoms using the first, second, and third harmonic left-handed circularly polarized radiation from the downstream part of the twin APPLE-II undulators. For each measurement, the peak photon energy of the corresponding harmonic in the undulator radiation was set to approximately 30 eV. While the first harmonic carries zero OAM, corresponding to plane-wave photons, the second and third harmonics carry OAM of $l\hbar$ per
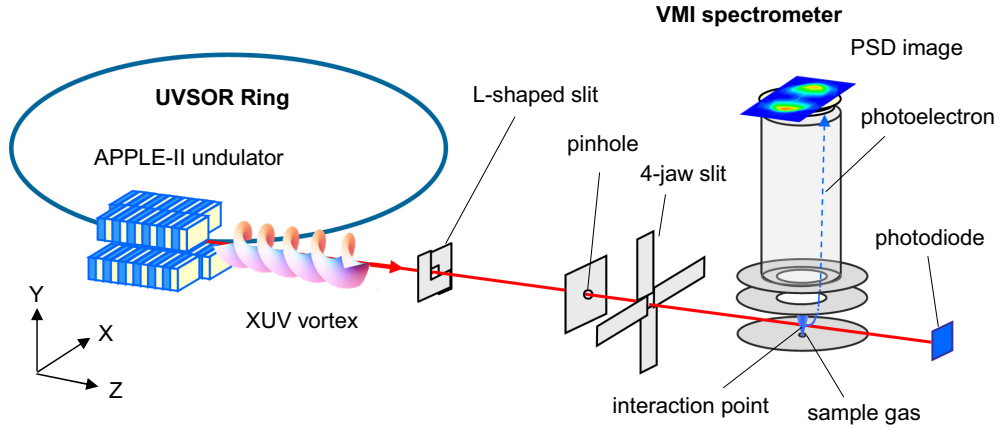
FIG. 1. Experimental setup used for the photoionization study of helium atoms using the XUV vortex. The XUV vortex generated by the APPLE-II undulator is introduced into the interaction point without any optical elements. Photoelectron angular distributions are obtained from the mapped electron image using the VMI spectrometer.

photon ($l = 1, 2$), along with a spin angular momentum of $\hbar$ per photon associated with the left-handed circular polarization.

The experimental setup is shown in Fig. 1. To avoid possible distortions of the helical wave front characterizing the XUV vortex, we did not use any optical elements in the experiment. The interaction point was placed at about 11 m downstream from the undulator, where the sample gas was admitted as an effusive beam from an aperture (diameter 300 μm). The central part of the photon beam from the undulator was cut out by a 1-mm-diameter pinhole located at the center of the photon beam, 0.5 m upstream of the interaction point. Since the radiation power of the helical undulator is minimum on axis, the pinhole position was adjusted to minimize the throughput beam intensity by scanning the pinhole in the transverse directions. The correspondence of the pinhole position to the beam center was checked whenever the undulator and storage ring parameters were changed. A pair of L-shaped knife edges positioned at the entrance of the beamline and a four-jaw slit downstream from the pinhole were used to suppress stray light entering into the interaction point.

We calculated the spatial intensity distribution and flux spectra of the photon beams at the interaction point using the simulation code SPECTRA [21]. The calculation was performed using the machine parameters of the UVSOR storage ring (750-MeV beam energy, 17.5 nm rad emittance, and 5% coupling) at 1 mA beam current. The left panels in Fig. 2 show the intensity distributions for 30 eV photons of the first, second, and third harmonics. While the intensity profile of the fundamental radiation forms a Gaussian-like distribution, annular distributions dominate the higher harmonic intensities, indicating their vortical nature. The nonzero intensities seen at the centers of the higher harmonics are due to the finite emittance of the electron beam. The intensity minimum resulting from the phase singularity becomes clearer when the electron beam emittance is much lower than the photon emittance [10,12]. Flux spectra calculated for transmission through a 1-mm-diameter pinhole are shown in the right panels of Fig. 2. The photon flux at 30 eV is reduced drastically for the higher harmonics, due to the cutout around the central axis of the undulator radiation. The photon energy bandwidths (FWHM) are estimated to be 2.2, 1.1, and 0.8 eV for the first,

second, and third harmonics, respectively. Fringe peaks are observed below and above the main peaks at 30 eV, and their contributions are larger for the higher harmonics.

Photoelectron angular distributions were measured by using a velocity map imaging (VMI) spectrometer [22]. Photoelectrons of about 6 eV kinetic energy emitted from helium atoms were detected by a two-dimensional position sensitive detector (PSD) having a detection area of 25 mm diameter. In order to eliminate background signal from secondary electrons emitted by photoion collisions with the electrode surface, a time window synchronized to the light pulse frequency was applied to the signals from the PSD. The raw images observed for photoelectrons created by the XUV vortex include non-negligible amounts of photoelectrons due to bending magnet radiation. This contribution was estimated by fully opening the pole gap of the undulator magnet to 200 mm to completely suppress undulator radiation, and subtracting the resulting signal from the raw images. After background subtraction, the angular and kinetic energy distributions of photoelectrons were obtained from the resulting images using the onion-peeling algorithm [23], assuming cylindrical symmetry around the light propagation axis (z direction).

III. RESULTS AND DISCUSSION

Figure 3 shows the background-subtracted images and kinetic energy distributions of photoelectrons from helium atoms measured for the first, second, and third harmonics, corresponding to plane-wave photons ($l = 0$), and XUV vortices of $l = 1$ and 2, respectively. The peak photon energies of the undulator radiation are about 31, 32, and 32 eV for the first, second, and third harmonics, respectively, as determined from the peak energies of the kinetic energy distributions. The photoelectron image for the first harmonic shows arc-shaped structures corresponding to photoelectrons produced by the main peak of the undulator radiation. The broadness of the photoelectron structure is mainly due to the bandwidth of the undulator radiation. The image shows a sizable intensity inside the arc structure, which is attributed to low-energy photoelectrons associated with the fringe structure seen in the undulator spectrum. As the fringe intensities are larger for the
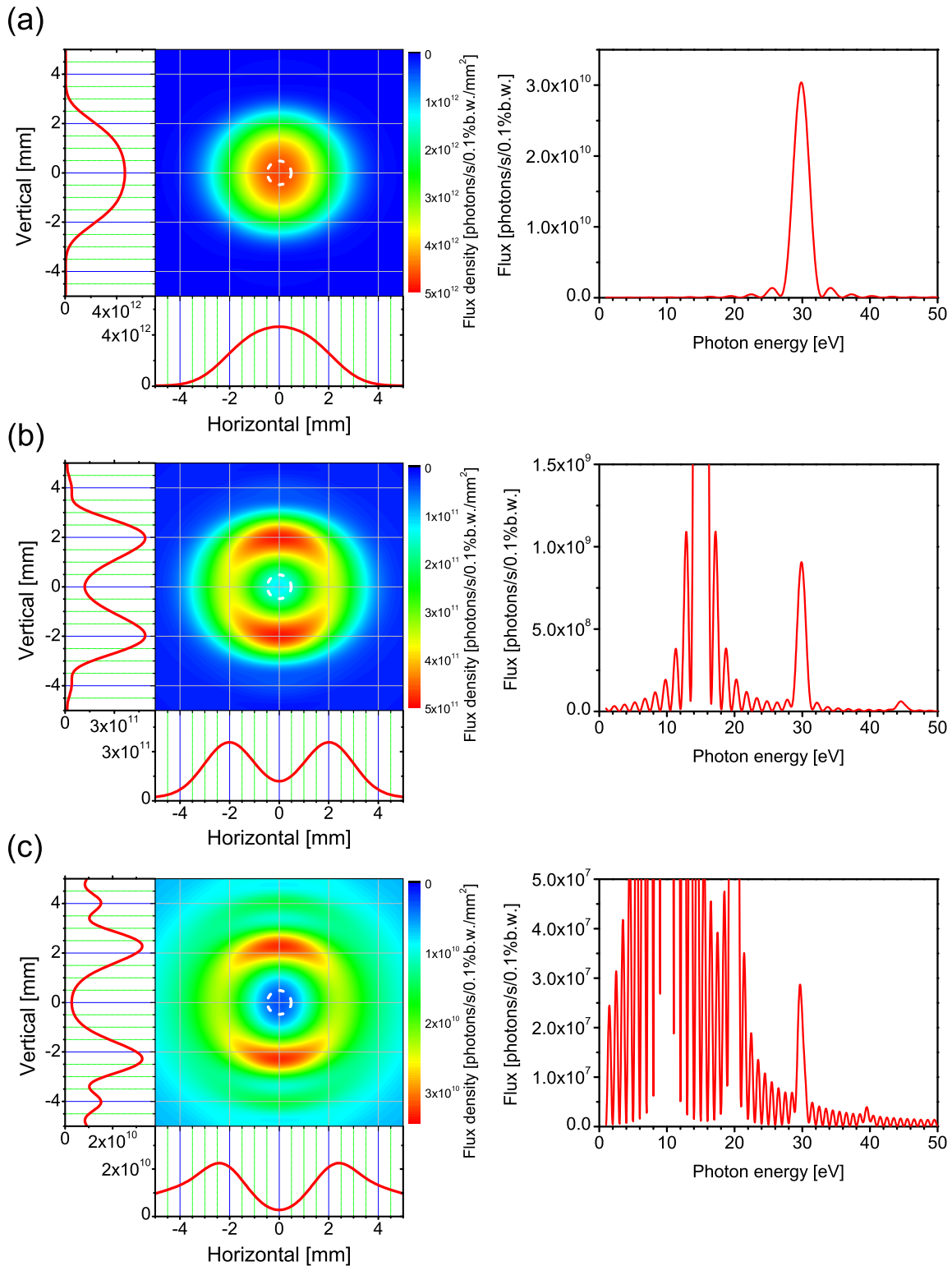
FIG. 2. Simulation of the undulator radiation at the interaction point for the (a) first, (b) second, and (c) third harmonics. Left: two-dimensional flux density plots in units of photons per second per 0.1% bandwidth (b.w.) per mm^2 for 30 eV photons. The intensity profiles along the horizontal and vertical center axes of the two-dimensional plots are attached. The first harmonic corresponds to a plane wave. The second and third harmonics correspond to XUV vortices carrying OAM of $l\hbar$ per photon with $l = 1$ and 2, respectively. For the harmonic radiation, the phase of the electromagnetic field changes according to the azimuthal angle around a zero-intensity minimum corresponding to the phase singularity on the propagation axis. In the present study, the zero-intensity minimum associated with the phase singularity is blurred due to the finite emittance of the electron beam. In the measurements, undulator radiation is cut out by a 1-mm-diameter pinhole. The cut out areas are indicted by dotted circles. Right: partial photon flux obtained for the undulator radiation passing through the 1-mm-diameter pinhole.
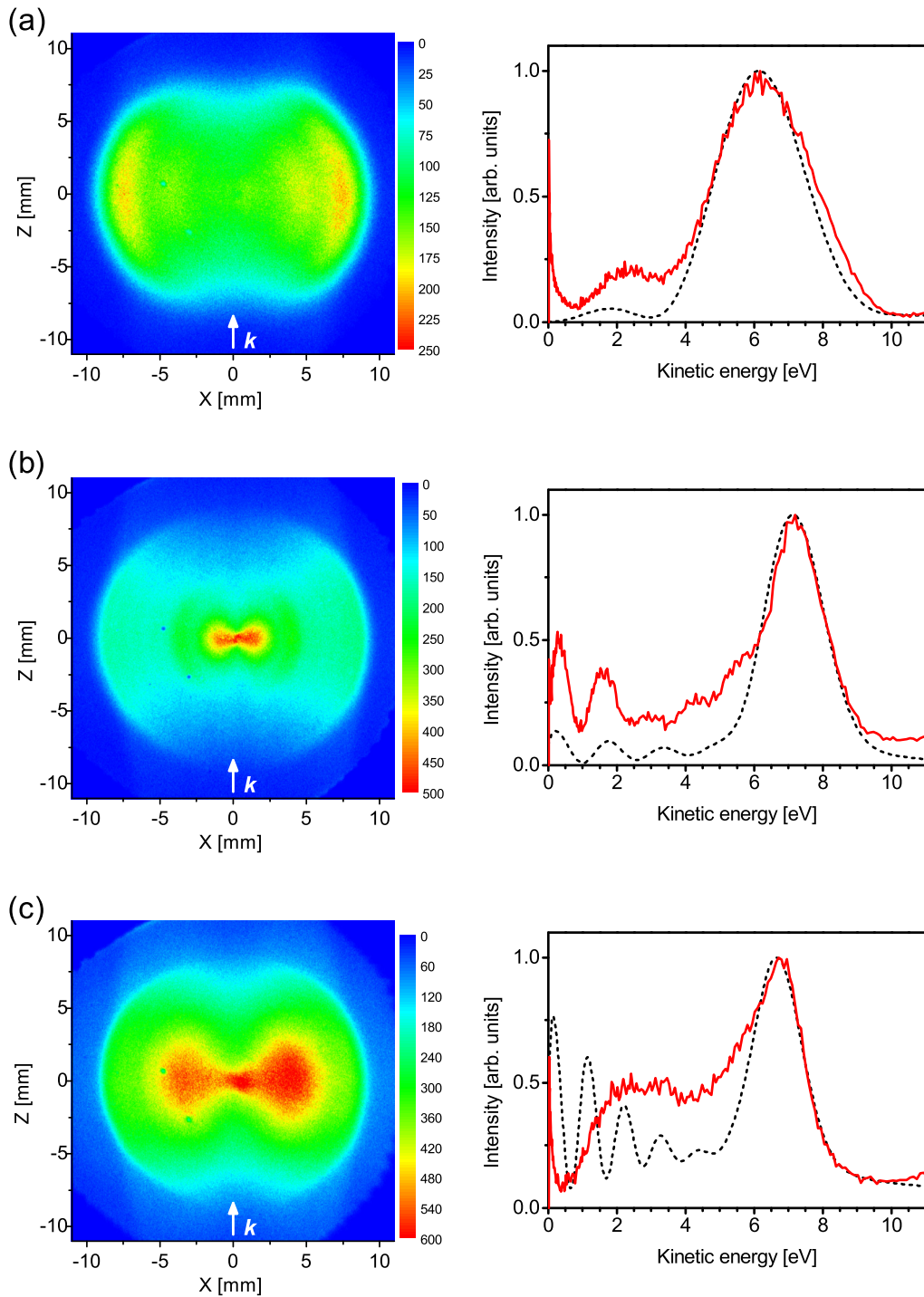
FIG. 3. Images and kinetic energy distributions of photoelectrons measured for the (a) first, (b) second, and (c) third harmonics from the helical undulator. The peak photon energies of the undulator radiation are 31, 32, and 32 eV for the first, second, and third harmonics, respectively. In the kinetic energy distributions, measurement and calculation results are plotted by solid red and dotted black curves, respectively.

higher harmonics (see Fig. 2), the photoelectron images for the second and third harmonics show large intensities inside the outermost arcs. In the right panels, the kinetic energy distributions are compared with the flux spectra weighted by the photoionization cross section [24]. The experimental resolution of the VMI spectrometer $\Delta E/E = 20\%$ (FWHM) is taken into account by convolution with a Gaussian line shape. The gross features of the experimentally observed kinetic energy distributions are fairly well reproduced by the calculation, confirming the validity of the observed images. Discrepancies between the experiments and calculations are seen for the fringe structures. This may be due to the fact that the nonsinusoidal magnetic fields formed by the actual end structures of the undulator magnets are not considered in the flux calculation.

For ordinary plane-wave light, the photon-atom interaction at XUV wavelengths is well described by the dipole
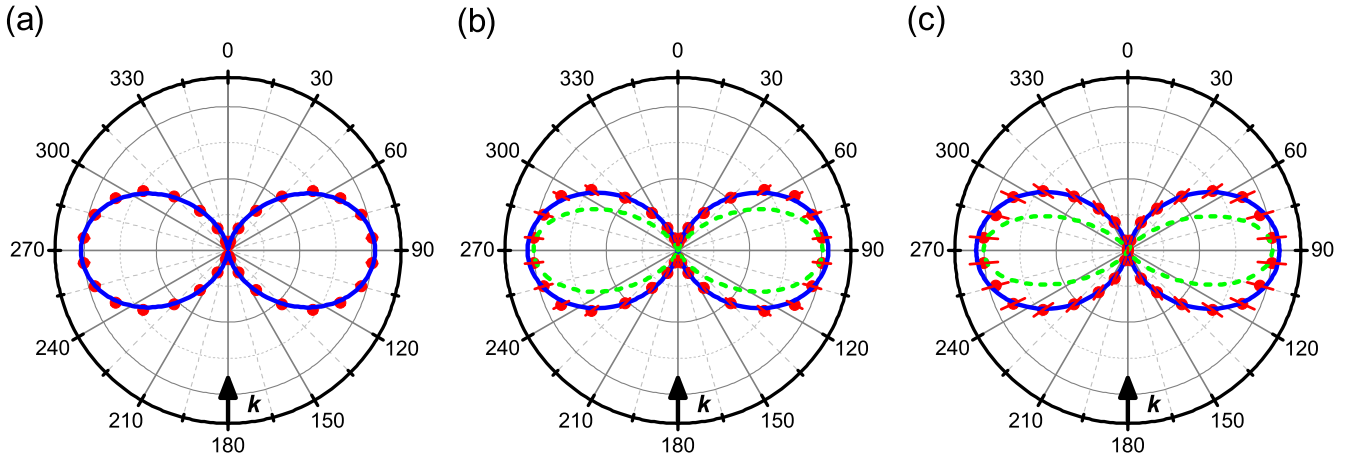
FIG. 4. Angular distributions of photoelectrons measured for the (a) first, (b) second, and (c) third harmonics from the helical undulator. The peak photon energies of the undulator radiation are 31, 32, and 32 eV for the first, second, and third harmonics, respectively. The solid blue curve in (a) represents a fit assuming electric dipole transitions. The dotted green curves in (b) and (c) show the angular dependence of the photoelectrons expected for nondipole transitions induced by the OAM carried by the XUV vortex. The solid blue curves in (b) and (c) represent fit results assuming both electric dipole and nondipole transitions.

approximation, since higher-order multipole terms are negligible [25]. Assuming the dipole approximation, the photoelectron angular distribution for circularly polarized light can be expressed as [26]

$$\frac{d\sigma}{d\Omega} = \frac{\sigma}{4\pi}\left[1 - \frac{1}{2}\beta P_2(\cos\theta)\right],$$

where σ is the cross section, β is the asymmetry parameter, and $P_2(\cos\theta)$ is the second-order Legendre polynomial. The emission angle θ is defined with respect to the light propagation axis. In contrast, according to the selection rule predicted for the interaction between OAM-carrying photons and atoms [15,19], one can expect that within the independent particle picture, the quadrupole transition of the helium $1s$ electron into the εd continuum ($\Delta l = +2$, $\Delta m = +2$) is allowed for the $l = 1$ vortex, leading to a $\sin^4\theta$ dependence in the photoelectron angular distribution, resulting from the square of the Y_{22} spherical harmonic in the wave function of the outgoing photoelectrons. Similarly, the octupole transition from $1s$ into the εf continuum ($\Delta l = +3$, $\Delta m = +3$) is allowed for the $l = 2$ vortex, and the photoelectron angular distribution is expected to be proportional to $\sin^6\theta$, from the square of the Y_{33} spherical harmonic.

Figure 4 shows the photoelectron angular distributions obtained for the main peaks in the kinetic energy distributions. The quadrants of each photoelectron image have been averaged to improve the statistics. The angular distribution measured for the first harmonic is well reproduced by the theoretical curve for the electric dipole transition. From curve fitting we obtain an asymmetry parameter of $\beta = 1.96 \pm 0.09$, in agreement with the theoretical value of $\beta = 2$ within the experimental uncertainty. This result confirms the high reliability of the present experimental and analytical methods for the study of photoelectron angular distributions using circularly polarized undulator radiation.

It can be seen from Figs. 4(b) and 4(c) that the angular distributions for photoionization by the XUV vortices do not follow the $\sin^4\theta$ and $\sin^6\theta$ angular distributions expected for nondipole transitions (dotted green lines in the figures), instead showing dipole patterns. To estimate the weak nondipole contributions to photoionization by the XUV vortex, we fit the observed distributions with functions, $I_D\sin^2\theta + I_Q\sin^4\theta$ and $I_D\sin^2\theta + I_O\sin^6\theta$ for the $l = 1$ and $l = 2$ XUV vortices, respectively, which represent simple sums of the ideal photoelectron angular distributions expected for the dipole and nondipole transitions. From curve fitting the dipole and nondipole components are determined to be $I_D = 1.04 \pm 0.06$, $I_Q = 0.00 \pm 0.07$ and $I_D = 1.05 \pm 0.02$, $I_O = 0.00 \pm 0.02$ for the $l = 1$ and $l = 2$ XUV vortices, respectively. The photoelectron angular distributions are well reproduced by the dipole components alone, and nondipole contributions are not detected within the experimental uncertainty—of the order of 10^{-2} relative to the normal dipole transitions.

This observation can be explained by considering the characteristics of nondipole transitions induced by OAM. As suggested by theoretical studies [15,19], the standard electric dipole selection rules fail, and nondipole transitions are allowed due to the OAM carried by the photon beam when the interacting atom is positioned at the phase singularity. This is because the nondipole transition arises from the change of the electric field strength around the atom due to the helical phase structure of the vortex. In the present experimental configuration, the gaseous sample is supplied by an effusive beam, resulting in helium atoms which are uniformly populated throughout the 1-mm-diameter photon beam. Thus the majority of photoelectrons come from helium atoms not located at the phase singularity, since the photon intensity increases in the radial direction. At distances far from the phase singularity, the phase of the XUV vortex beam is near constant across the atom, leading to an approximately plane-wave field. Consequently, the photon-atom interaction will be well described by the normal dipole approximation. The helical phase effect on atomic transitions is predicted to be significant only on a distance scale comparable to

the wavelength of the radiation [17,18]. Thus we conclude that while nondipole contributions must exist in the present measurements, they remain hidden behind the dominant dipole photoionization, and are undetectable even with the small experimental uncertainties. Our result indicates that nondipole interactions induced by OAM are not observable in conventional gas-phase experiments using a synchrotron light source.

We note further that a blurring of the phase singularity occurs due to the finite emittance of the electron beam. The XUV vortices used in the present experiment have nonzero intensities on the axis (see Fig. 2). This spatial property results from the incoherent overlap of the radiation from electrons passing through the undulator, although the radiation from each electron has a zero-intensity minimum and an individual phase singularity. Thus the nondipole components will be veiled by the electric dipole transitions, even for an atom located precisely at the intensity minimum of the present XUV vortex.

From the perspective of a single photon, one may consider that the total OAM of the interacting photon-atom system is not preserved in the present measurement, since the atomic absorption of a photon with nonzero OAM results in a normal electric dipole transition. This is essentially due to the properties of OAM, which depends on the choice of axis. The OAM of $l\hbar$ carried by the photons is originally defined with respect to the phase singularity of the vortex. For atomic transitions, however, the effective OAM of the photon should be defined with respect to the nucleus of the interacting atomic system. Therefore, for an atom located far from the phase singularity, the OAM of the photon is calculated for the plane-wave field around the nucleus, giving zero OAM. On the other hand, when the interacting atom is placed at the phase singularity, the OAM of $l\hbar$ carried by the photon is preserved in the photon-atom system, allowing nondipole transitions.

IV. CONCLUSION

In conclusion, we have demonstrated the limitations in photoionization of atoms interacting with an XUV vortex. The atom-vortex interaction was dominated by normal dipole transitions under the present experimental conditions: helium atoms with a broad spatial distribution were ionized by an XUV vortex of 1 mm diameter at about 30 eV photon energy. Nondipole contributions were not detected within an experimental uncertainty of the order of 10^{-2} relative to the normal dipole transitions. The present result indicates that both a photon beam with a single well-defined phase singularity and the localization of sample atoms near the phase singularity are required to selectively observe nondipole transitions. Such an XUV vortex could be obtained by a diffraction-limited storage ring [27] with an electron beam emittance less than 1 nm rad, much lower than the photon emittance in the XUV region. Another candidate is the production of a coherent optical vortex utilizing various schemes based on free electron lasers [28,29] and on high-harmonic generation by ultrashort laser pulses [30,31]. In combination with localized samples prepared by atom trapping or laser excitation, the specific features of the interaction between OAM-carrying photons and atoms in the XUV and shorter wavelengths will be explored in future experiments.

[1] L. Allen, M. W. Beijersbergen, R. J. C. Spreeuw, and J. P. Woerdman, Phys. Rev. A **45**, 8185 (1992).

[2] J. Wang, J.-Y. Yang, I. M. Fazal, N. Ahmed, Y. Yan, H. Huang, Y. Ren, Y. Yue, S. Dolinar, M. Tur, and A. E. Willner, Nat. Photonics **6**, 488 (2012).

[3] M. Padgett and R. Bowman, Nat. Photonics **5**, 343 (2011).

[4] J. H. Lee, G. Foo, E. G. Johnson, and G. A. Swartzlander, Jr., Phys. Rev. Lett. **97**, 053901 (2006).

[5] S. Hell, Nat. Biotechnol. **21**, 1347 (2003).

[6] A. M. Yao and M. J. Padgett, Adv. Opt. Photonics **3**, 161 (2011).

[7] A. G. Peele, K. A. Nugent, A. P. Mancuso, D. Paterson, I. McNulty, and J. P. Hayes, J. Opt. Soc. Am. A **21**, 1575 (2004).

[8] A. Sakdinawat and Y. Liu, Opt. Lett. **32**, 2635 (2007).

[9] Y. Kohmura, K. Sawada, M. Taguchi, T. Ishikawa, T. Ohigashi, and Y. Suzuki, Appl. Phys. Lett. **94**, 101112 (2009).

[10] S. Sasaki and I. McNulty, Phys. Rev. Lett. **100**, 124801 (2008).

[11] J. Bahrdt, K. Holldack, P. Kuske, R. Müller, M. Scheer, and P. Schmid, Phys. Rev. Lett. **111**, 034801 (2013).

[12] S. Sasaki, A. Miyamoto, M. Hosaka, N. Yamamoto, T. Konomi, and M. Katoh, in *Proceedings of the International Particle Accelerator Conference (IPAC), Richmond, VA, 2015* (JACow, CERN, Geneva, 2015), p. 1563.

[13] M. Katoh *et al.*, arXiv:1609.03869.

[14] M. Katoh, M. Fujimoto, H. Kawaguchi, K. Tsuchiya, K. Ohmi, T. Kaneyasu, Y. Taira, M. Hosaka, A. Mochihashi, and Y. Takashima, Phys. Rev. Lett. (to be published).

[15] A. Picón, A. Benseny, J. Mompart, J. R. V. de Aldana, L. Plaja, G. F. Calvo, and L. Roso, New J. Phys. **12**, 083053 (2010).

[16] C. T. Schmiegelow and F. Schmidt-Kaler, Eur. Phys. J. D **66**, 157 (2012).

[17] O. Matula, A. G. Hayrapetyan, V. G. Serbo, A. Surzhykov, and S. Fritzsche, J. Phys. B: At., Mol. Opt. Phys. **46**, 205002 (2013).

[18] A. Afanasev, C. E. Carlson, and A. Mukherjee, Phys. Rev. A **88**, 033841 (2013).

[19] J. D. Rodrigues, L. G. Marcassa, and J. T. Mendonça, J. Phys. B: At., Mol. Opt. Phys. **49**, 074007 (2016).

[20] M. van Veenendaal and I. McNulty, Phys. Rev. Lett. **98**, 157401 (2007).

[21] T. Tanaka and H. Kitamura, J. Synchrotron Radiat. **8**, 1221 (2001).

[22] Y. Hikosaka and E. Shigemasa, J. Electron Spectrosc. Relat. Phenom. **148**, 5 (2005).

[23] S. Manzhos and H. P. Loock, Comput. Phys. Commun. **154**, 76 (2003).

[24] J. M. Bizau and F. J. Wuilleumier, J. Electron Spectrosc. Relat. Phenom. **71**, 205 (1995).

[25] H. A. Bethe and E. E. Salpeter, *Quantum Mechanics of One- and Two-Electron Atoms* (Springer-Verlag, Berlin, 1957).

[26] M. Peshkin, in *Advances in Chemical Physics*, edited by I. Prigogine and Stuart A. Rice (Interscience, New York, 1970), Vol. 18, pp. 1–14.

[27] M. Eriksson, J. Synchrotron Radiat. **21**, 837 (2014).

[28] E. Hemsing, A. Marinelli, and J. B. Rosenzweig, Phys. Rev. Lett. **106**, 164803 (2011).

[29] P. R. Ribič, D. Gauthier, and G. De Ninno, Phys. Rev. Lett. **112**, 203602 (2014).

[30] G. Gariepy, J. Leach, K. T. Kim, T. J. Hammond, E. Frumker, R. W. Boyd, and P. B. Corkum, Phys. Rev. Lett. **113**, 153901 (2014).

[31] M. Zürch, C. Kern, P. Hansinger, A. Dreischuh, and C. Spielmann, Nat. Phys. **8**, 743 (2012).